Cold-fluid equilibrium for a corkscrewing elliptic beam in a variably focusing channel

Renato Pakter* and Chiping Chen
Plasma Science and Fusion Center, Massachusetts Institute of Technology, Cambridge, Massachusetts 02139
(Received 5 November 1999; revised manuscript received 5 April 2000)

It is shown that there exists a new class of cold-fluid corkscrewing elliptic beam equilibria for ultrahigh-brightness, space-charge-dominated beam propagation through a linear focusing channel consisting of uniform solenoidal, periodic solenoidal, and/or alternating-gradient quadrupole focusing magnets in an arbitrary arrangement including field tapering. The equilibrium beam density and flow velocity profiles and equilibrium self-electric and self-magnetic fields are determined by solving generalized beam envelope equations. In proper limits, such cold-fluid corkscrewing elliptic beam equilibria recover many familiar beam equilibria in beam physics, including the round rigid-rotor Vlasov beam equilibria in uniform and periodic solenoidal focusing fields and the Kapchinskij-Vladimirskij beam equilibrium in an alternating-gradient quadrupole focusing field. For beams with negligibly small emittance, the equilibrium solutions are validated with self-consistent simulations. Examples and applications of the present equilibrium beam theory are discussed. As an important application of the present equilibrium beam theory, a general technique is developed and demonstrated with an example to control large-amplitude density and flow velocity fluctuations (such as beam hollowing and halo formation) often observed in ultrahigh-brightness beams.

PACS number(s): 29.27.−a, 41.75.−i, 41.85.−p

I. INTRODUCTION

The equilibrium and stability properties of charged-particle beams have been an important subject of investigation in beam physics, plasma physics, and vacuum electronics. Indeed, the principles of vacuum electronics [1] are based on electron beam interactions with radio-frequency structures, and the discovery of strong focusing in the early 1950s [2] has provided the scientific basis for modern particle accelerators such as synchrotrons, linacs, and high-energy colliders.

Recently, there have been vigorous activities in the research and development of high-intensity vacuum electronic devices and high-intensity accelerators in order to meet the needs in communication, in high-energy and nuclear physics research, in the development of spallation neutron sources, in heavy ion fusion applications, and in advanced x-ray radiography, to mention a few examples.

In the design of high-intensity charged-particle beam systems, the most challenging task is to properly match high-intensity beams into focusing systems, so that the beams are in equilibrium or quasiequilibrium states in the combination of applied fields and self-fields [3]. A widely used tool for the determination of matching conditions of high-intensity charged-particle beam systems is based on the rms beam description [4–7]. However, rms beam matching is inadequate for ultrahigh-brightness beams, because detailed information about the beam dynamics, especially the evolution of the density and flow velocity profiles, is lost by performing phase-space averages in the rms analysis. In general, rms beam matching does not guarantee well-behaved beam transport if the beam becomes space-charge dominated. In fact, without detailed equilibrium flow matching of high-intensity beams, many undesirable phenomena can occur, including chaotic particle motion [8] and chaotic beam envelope oscillations [9], beam halo formation [10], beam hollowing [11], emittance growth [12], and multimode excitations, as observed in recent high-intensity beam experiments.

In this paper, we present exact steady-state solutions to the cold-fluid equations governing the evolution of an ultrahigh-brightness, space-charge-dominated beam propagating through a linear focusing channel consisting of uniform solenoidal, periodic solenoidal, and alternating-gradient quadrupole focusing magnets in an arbitrary arrangement including field tapering. The equilibrium beam density and flow velocity profiles and equilibrium self-electric and self-magnetic fields are determined by solving generalized beam envelope equations. For beams with negligibly small emittance, these steady-state solutions are validated with self-consistent simulations using the Green's function method. In general, these steady-state solutions correspond to corkscrewing elliptic beam equilibria. They recover many familiar beam equilibria in beam physics, such as the cold-fluid round rigid-rotor equilibrium [13,14] and both the periodically focused rigid-rotor Vlasov equilibrium [15] and Kapchinskij-Vladimirskij equilibrium [16] in the zero-emittance limit.

Examples and applications of the present equilibrium beam theory are discussed. As a simple example, a corkscrewing elliptic beam equilibrium in a uniform solenoidal magnetic field is obtained. As an important application of the present equilibrium beam theory, a general technique is developed and demonstrated with an example to control large-amplitude density and flow velocity fluctuations (such as beam hollowing and halo formation) often observed in ultrahigh-brightness beams. For comparison, we investigate numerically the beam transport for distributions that substantially deviate from the equilibrium solutions. In this case, the occurrence of beam hollowing and halo formation is found. As a final example, we consider an ultrahigh-brightness beam equilibrium in a periodic focusing channel consisting

*Present address: Instituto de Fisica, Universidade Federal do Rio Grande do Sul, Caixa Postal 15051, 91501-970 Porto Alegre, RS, Brazil.

 ©2000 The American Physical Society

of overlapping solenoidal and quadrupole focusing fields to illustrate a wide range of applicability of the present equilibrium beam theory in manipulating ultrahigh-brightness beams.

The paper is organized as follows. In Sec. II, steady-state cold-fluid equations are presented for transverse electrostatic and magnetostatic interactions in a high-intensity charged-particle beam propagating through a linear focusing channel with general magnetic focusing field profile. In Sec. III, an equilibrium solution to the steady-state cold-fluid equations presented in Sec. II is obtained and generalized beam envelope equations for equilibrium flow are derived. In Sec. IV, it is shown that the steady-state cold-fluid solutions found in Sec. III recover familiar beam equilibria in proper limits. In Sec. V, examples and applications of the present equilibrium beam theory are discussed. Conclusions are given in Sec. VI.

II. THEORETICAL MODEL AND ASSUMPTIONS

We consider a thin, continuous, ultrahigh-brightness, space-charge-dominated beam propagating with constant axial velocity $\beta_b c\hat{\mathbf{e}}_z$ through a linear focusing channel with multiple periodic solenoidal and alternating-gradient quadrupole focusing sections. The focusing fields can be tapered, and the quadrupoles are allowed to be at various angles in the transverse direction. The focusing magnetic field is approximated by

$$\mathbf{B}_0(\mathbf{x})=B_z(s)\hat{\mathbf{e}}_z-\frac{1}{2}B_z'(s)(x\hat{\mathbf{e}}_x+y\hat{\mathbf{e}}_y)+(\partial B_x^q/\partial\bar{y})_0(\bar{y}\hat{\mathbf{e}}_{\bar{x}}+\bar{x}\hat{\mathbf{e}}_{\bar{y}}), \tag{1}$$

where $B_z'(s)=(\partial B_z/\partial s)_0$, $s=z$ is the axial coordinate, $\bar{x}$, $\bar{y}$, $\hat{\mathbf{e}}_{\bar{x}}$, and $\hat{\mathbf{e}}_{\bar{y}}$ are coordinates and unit vectors of a frame of reference that is rotated by an angle of φ_q with respect to the x axis in the laboratory frame, $(\partial B_x^q/\partial\bar{y})_0=(\partial B_y^q/\partial\bar{x})_0$, and the subscript ''zero'' denotes $(x,y)=0=(\bar{x},\bar{y})$.

In the present analysis, we consider the transverse electrostatic and magnetostatic interactions in the beam. We make the usual paraxial approximation, assuming that (a) the Budker parameter is small compared with γ_b, i.e., $q^2N_b/\gamma_b mc^2\ll 1$, (b) the beam is thin compared with the characteristic length scale over which the beam envelope varies, and (c) the kinetic energy associated with the transverse particle motion is small compared with that associated with the axial particle motion.

For an ultrahigh-brightness beam, kinetic (emittance) effects are negligibly small, and the beam can be adequately described by cold-fluid equations. In the paraxial approximation, the steady-state cold-fluid equations for time-stationary flow $(\partial/\partial t=0)$ are

$$\beta_b c\frac{\partial}{\partial s}n_b+\boldsymbol{\nabla}_\perp\cdot(n_b\mathbf{V}_\perp)=0, \tag{2}$$

$$\nabla_\perp^2\phi^s=\beta_b^{-1}\nabla_\perp^2A_z^s=-4\pi qn_b, \tag{3}$$

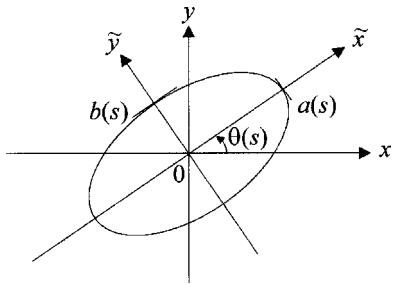

FIG. 1. Laboratory and rotating coordinate systems.

$$n_b\left(\beta_b c\frac{\partial}{\partial s}+\mathbf{V}_\perp\cdot\frac{\partial}{\partial\mathbf{x}_\perp}\right)\mathbf{V}_\perp=\frac{qn_b}{\gamma_b m}\left[-\frac{1}{\gamma_b^2}\boldsymbol{\nabla}_\perp\phi^s+\beta_b\hat{\mathbf{e}}_z\times\mathbf{B}_{0\perp}+\frac{\mathbf{V}_\perp}{c}\times B_z(s)\hat{\mathbf{e}}_z\right], \tag{4}$$

where $\mathbf{x}_\perp=x\hat{\mathbf{e}}_x+y\hat{\mathbf{e}}_y$, $\gamma_b=(1-\beta_b^2)^{-1/2}$, and the self-electric and self-magnetic fields $\mathbf{E}^s$ and $\mathbf{B}^s$ are determined from the scalar and vector potentials ϕ_s and $A_z^s\hat{\mathbf{e}}_z$, i.e., $\mathbf{E}^s=-\boldsymbol{\nabla}_\perp\phi^s$ and $\mathbf{B}^s=\boldsymbol{\nabla}\times A_z^s\hat{\mathbf{e}}_z$. In Sec. III, it will be shown that the steady-state cold-fluid equations (2)–(4) support a class of solutions that, in general, describe corkscrewing elliptic beam equilibria in the magnetic focusing field defined in Eq. (1).

III. CORKSCREWING BEAM EQUILIBRIUM

In this section, we show that there exists a class of solutions to the steady-state cold-fluid equations (2)–(4) which, in general, describe corkscrewing elliptic beam equilibria for ultrahigh-brightness, space-charge-dominated beam propagation in the linear focusing channel defined in Eq. (1).

We seek solutions to Eqs. (2)–(4) of the form

$$n_b(\mathbf{x}_\perp,s)=\frac{N_b}{\pi a(s)b(s)}\Theta\left[1-\frac{\tilde{x}^2}{a^2(s)}-\frac{\tilde{y}^2}{b^2(s)}\right], \tag{5}$$

$$\mathbf{V}_\perp(\mathbf{x}_\perp,s)=[\mu_x(s)\tilde{x}-\alpha_x(s)\tilde{y}]\beta_b c\hat{\mathbf{e}}_{\tilde{x}}+[\mu_y(s)\tilde{y}+\alpha_y(s)\tilde{x}]\beta_b c\hat{\mathbf{e}}_{\tilde{y}}. \tag{6}$$

In Eqs. (5) and (6), $\mathbf{x}_\perp=\tilde{x}\hat{\mathbf{e}}_{\tilde{x}}+\tilde{y}\hat{\mathbf{e}}_{\tilde{y}}$ is a transverse displacement in a rotating frame illustrated in Fig. 1, $\theta(s)$ is the angle of rotation of the ellipse with respect to the laboratory frame, $\Theta(x)=1$ if $x>0$ and $\Theta(x)=0$ if $x<0$, and the functions $a(s)$, $b(s)$, $\mu_x(s)$, $\mu_y(s)$, $\alpha_x(s)$, $\alpha_y(s)$, and $\theta(s)$ are to be determined self-consistently.

Substituting Eqs. (5) and (6) into Eq. (2) and expressing the result in terms of the tilded variables, we find

$$\left(\mu_x+\mu_y-\frac{a'}{a}-\frac{b'}{b}\right)\Theta\left[1-\frac{\tilde{x}^2}{a^2}-\frac{\tilde{y}^2}{b^2}\right]+2\left[\left(\frac{a'}{a}-\mu_x\right)\frac{\tilde{x}^2}{a^2}+\left(\frac{b'}{b}-\mu_y\right)\frac{\tilde{y}^2}{b^2}+\left(-\frac{b\theta'}{a}+\frac{a\theta'}{b}+\frac{b\alpha_x}{a}-\frac{a\alpha_y}{b}\right)\frac{\tilde{x}\tilde{y}}{ab}\right]\times\delta\left[1-\frac{\tilde{x}^2}{a^2}-\frac{\tilde{y}^2}{b^2}\right]=0, \tag{7}$$

where the prime denotes derivative with respect to s, $\delta(x) \equiv d\Theta(x)/dx$, and use has been made of the identities $\partial\tilde{x}/\partial s = \theta'\tilde{y}$, $\partial\tilde{y}/\partial s = -\theta'\tilde{x}$, and $\boldsymbol{\nabla}\cdot\mathbf{F} = \partial F_{\tilde{x}}/\partial\tilde{x} + \partial F_{\tilde{y}}/\partial\tilde{y}$ for any vector field $\mathbf{F}$. Since Eq. (7) must be satisfied for all $\tilde{x}$ and $\tilde{y}$, the coefficients of the terms proportional to Θ, $\tilde{x}^2\delta$, $\tilde{y}^2\delta$, and $\tilde{x}\tilde{y}\delta$, must vanish independently. This leads to the following equations:

$$\mu_x = \frac{1}{a}\frac{da}{ds}, \quad \mu_y = \frac{1}{b}\frac{db}{ds}, \tag{8}$$

$$\frac{d\theta}{ds} = \frac{a^2\alpha_y - b^2\alpha_x}{a^2 - b^2}, \tag{9}$$

where the functions $a(s)$, $b(s)$, $\alpha_x(s)$, and $\alpha_y(s)$ still remain to be determined.

Solving for the scalar and vector potentials from Eq. (3), we obtain

$$\phi^s = \beta_b^{-1} A_z^s = -\frac{2qN_b}{a+b}\left(\frac{\tilde{x}^2}{a} + \frac{\tilde{y}^2}{b}\right) \tag{10}$$

in the beam interior with $\tilde{x}^2/a^2 + \tilde{y}^2/b^2 < 1$. In deriving Eq. (10), use has been made of $\nabla_\perp^2 = \partial^2/\partial\tilde{x}^2 + \partial^2/\partial\tilde{y}^2$.

To solve the force equation (4), we substitute Eqs. (5), (6), and (8)–(10) into Eq. (4), express the results in terms of the tilded variables, and use the relations $\partial\tilde{x}/\partial s = \theta'\tilde{y}$, $\partial\tilde{y}/\partial s = -\theta'\tilde{x}$, $\partial\hat{\mathbf{e}}_{\tilde{x}}/\partial s = \theta'\hat{\mathbf{e}}_{\tilde{y}}$, and $\partial\hat{\mathbf{e}}_{\tilde{y}}/\partial s = -\theta'\hat{\mathbf{e}}_{\tilde{x}}$. We obtain

$$\{f_x + \kappa_q\cos[2(\theta-\varphi_q)]\}\tilde{x} - \{g_y + \kappa_q\sin[2(\theta-\varphi_q)]\}\tilde{y} = 0, \tag{11a}$$

$$\{g_x - \kappa_q\sin[2(\theta-\varphi_q)]\}\tilde{x} + \{f_y - \kappa_q\cos[2(\theta-\varphi_q)]\}\tilde{y} = 0 \tag{11b}$$

in the $\tilde{x}$ and $\tilde{y}$ directions, respectively. In Eq. (11),

$$f_x = \frac{1}{a}\frac{d^2a}{ds^2} - \frac{b^2(\alpha_x^2 - 2\alpha_x\alpha_y) + a^2\alpha_y^2}{a^2-b^2} - 2\alpha_y\sqrt{\kappa_z} - \frac{2K}{a(a+b)}, \tag{12a}$$

$$f_y = \frac{1}{b}\frac{d^2b}{ds^2} + \frac{a^2(\alpha_y^2 - 2\alpha_x\alpha_y) + b^2\alpha_x^2}{a^2-b^2} - 2\alpha_x\sqrt{\kappa_z} - \frac{2K}{b(a+b)}, \tag{12b}$$

$$g_y = \frac{1}{b^2}\left\{\frac{d}{ds}[b^2(\alpha_x + \sqrt{\kappa_z})] - \frac{a^3b(\alpha_x-\alpha_y)}{a^2-b^2}\frac{d}{ds}\left(\frac{b}{a}\right)\right\}, \tag{12c}$$

$$g_x = \frac{1}{a^2}\left\{\frac{d}{ds}[a^2(\alpha_y + \sqrt{\kappa_z})] - \frac{ab^3(\alpha_x-\alpha_y)}{a^2-b^2}\frac{d}{ds}\left(\frac{a}{b}\right)\right\}. \tag{12d}$$

Since Eqs. (11a) and (11b) must be satisfied for all $\tilde{x}$ and $\tilde{y}$, we obtain the generalized beam envelope equations

$$f_x + \kappa_q\cos[2(\theta-\varphi_q)] = 0, \tag{13a}$$

$$f_y - \kappa_q\cos[2(\theta-\varphi_q)] = 0, \tag{13b}$$

$$g_y + \kappa_q\sin[2(\theta-\varphi_q)] = 0, \tag{13c}$$

$$g_x - \kappa_q\sin[2(\theta-\varphi_q)] = 0. \tag{13d}$$

Making use of Eq. (12), we can express the generalized beam envelope equations as [17]

$$\frac{d^2a}{ds^2} + \left\{\kappa_q(s)\cos[2(\theta-\varphi_q)] - \frac{b^2(\alpha_x^2 - 2\alpha_x\alpha_y) + a^2\alpha_y^2}{a^2-b^2} - 2\alpha_y\sqrt{\kappa_z}\right\}a - \frac{2K}{(a+b)} = 0, \tag{14a}$$

$$\frac{d^2b}{ds^2} + \left\{-\kappa_q(s)\cos[2(\theta-\varphi_q)] + \frac{a^2(\alpha_y^2 - 2\alpha_x\alpha_y) + b^2\alpha_x^2}{a^2-b^2} - 2\alpha_x\sqrt{\kappa_z}\right\}b - \frac{2K}{(a+b)} = 0, \tag{14b}$$

$$\frac{d}{ds}[b^2(\alpha_x + \sqrt{\kappa_z})] - \frac{a^3b(\alpha_x-\alpha_y)}{a^2-b^2}\frac{d}{ds}\left(\frac{b}{a}\right) + \kappa_q(s)b^2\sin[2(\theta-\varphi_q)] = 0, \tag{14c}$$

$$\frac{d}{ds}[a^2(\alpha_y + \sqrt{\kappa_z})] - \frac{ab^3(\alpha_x-\alpha_y)}{a^2-b^2}\frac{d}{ds}\left(\frac{a}{b}\right) - \kappa_q(s)a^2\sin[2(\theta-\varphi_q)] = 0, \tag{14d}$$

$$\frac{d\theta}{ds} - \frac{a^2\alpha_y - b^2\alpha_x}{a^2-b^2} = 0, \tag{14e}$$

$$\mu_x = \frac{1}{a}\frac{da}{ds}, \tag{14f}$$

$$\mu_y = \frac{1}{b}\frac{db}{ds}. \tag{14g}$$

Equations (8) and (9) are added here as Eqs. (14e)–(14g) for completeness. Equations (14a)–(14g), together with the density and velocity profiles defined in Eqs. (5) and (6), describe cold-fluid equilibrium states for variably focused ultrahigh-brightness beams.

IV. LIMITING CASES

A wide variety of cold-fluid beam equilibria can be constructed with Eqs. (5), (6), and (14) for proper choices of magnetic focusing field profiles. While cold-fluid beam equilibria are elliptic and corkscrewing in general, they do recover familiar beam equilibria in proper limits. In this section, we discuss some of these limiting cases.

First, let us consider the case of an axisymmetric beam in a periodic solenoidal focusing field with $\kappa_z(s) = \kappa_z(s+S) \neq 0$, $\kappa_q(s) = 0$, and $a(s) = a(s+S) = b(s)$. In this limit, Eqs. (14c)–(14e) imply that

$$\frac{d\theta}{ds} = \alpha_x = \alpha_y = \frac{\varepsilon_d}{a^2(s)} - \sqrt{\kappa_z(s)}, \tag{15}$$

where $\varepsilon_d = \text{const}$ is an unnormalized emittance associated with beam rotation relative to the Larmor frequency $\sqrt{\kappa_z(s)}$. Equation (15) indicates that the beam rotates at a rate that is

a periodic function of the axial propagation distance s. Substituting Eq. (15) into Eqs. (14a) and (14b), setting $\alpha_x = \alpha_y$, and taking the limit $a = b$, it is readily shown that the beam envelope equations reduce to

$$\frac{d^2a}{ds^2} + \kappa_z(s)a - \frac{K}{a} - \frac{\varepsilon_d^2}{a^3} = 0. \tag{16}$$

The equilibrium described by Eqs. (5), (6), (15), and (16) is identical to the familiar round rigid-rotor Vlasov beam equilibrium [15] in the zero-emittance limit.

Second, in a uniform magnetic focusing field with $\kappa_z(s) = \kappa_{z0} = \text{const}$, $\kappa_q(s) = 0$, and $a(s) = b(s)$, a special solution to the beam envelope equation (16) is

$$a = \left[\frac{K + (K^2 + 4\kappa_{z0}\varepsilon_d^2)^{1/2}}{2\kappa_{z0}}\right]^{1/2} = \text{const}, \tag{17}$$

and the equilibrium recovers the familiar cold-fluid round rigid-rotor beam equilibrium [13,14]. A general class of corkscrewing elliptical beam equilibria with constant radii $a \neq b$ in a uniform solenoidal focusing field is discussed in detail in Sec. IV A.

As a third limiting case, we consider a nonrotating elliptical beam in an alternating-gradient quadrupole focusing field with $\kappa_z(s) = 0$, $\kappa_q(s) = \kappa_q(s+S)$, $\theta(s) = 0$, $a(s) = a(s+S)$, $b(s) = b(s+S)$, and $\alpha_x(s) = \alpha_y(s) = 0$. In this case, Eqs. (14c)–(14e) are automatically satisfied and the envelope equations reduce to

$$\frac{d^2a}{ds^2} + \kappa_q(s)a - \frac{2K}{a+b} = 0, \tag{18a}$$

$$\frac{d^2b}{ds^2} - \kappa_q(s)b - \frac{2K}{a+b} = 0. \tag{18b}$$

Note that the internal flow must satisfy $\alpha_x(s) = \alpha_y(s) = 0$ in order to prevent the beam from rotating with a finite $d\theta/ds$. The equilibrium described by Eqs. (5), (6), and (18) correspond to the familiar Kapchinskij-Vladimirskij beam equilibrium [16] in alternating-gradient quadrupole magnetic focusing field in the zero-emittance limit.

V. EXAMPLES AND APPLICATIONS

In this section, we discuss three examples of cold-fluid corkscrewing elliptic beam equilibria predicted by the equilibrium beam theory presented in Sec. IV. These examples are (a) cold-fluid corkscrewing elliptic beam equilibria in a uniform magnetic field (Sec. V A), (b) matching and transport of an ultrahigh-brightness round beam generated by an axisymmetric particle source into an alternating-gradient magnetic quadrupole focusing channel (Sec. V B), and (c) matching and transport of an ultrahigh-brightness round beam into a periodic focusing channel consisting of overlapping solenoidal and quadrupole focusing fields (Sec. V C).

In addition to illustrating a large class of beam equilibria predicted by the present equilibrium beam theory, these examples are also intended to demonstrate a general technique for controlling of large-amplitude beam density and flow velocity fluctuations and associated emittance growth and beam halo formation often observed in ultrahigh-brightness beam experiments. To demonstrate the efficacy of this beam control technique, the transport for an ultrahigh-brightness beam with an initial perturbation about the equilibrium transverse flow velocity is compared with the equilibrium beam transport (Sec. V B).

A. Corkscrewing elliptic beam equilibria in a uniform magnetic field

As a simple example, we consider corkscrewing elliptic beam equilibria in a uniform magnetic field with $\mathbf{B}^{\text{ext}} = B_{z0}\hat{\mathbf{e}}_z$. Setting $\sqrt{\kappa_z(s)} = \sqrt{\kappa_{z0}} = qB_{z0}/2\gamma_b\beta_b mc^2 = \text{const}$ and $\kappa_q(s) = 0$, it can be shown that Eq. (14) has the following two branches of physically acceptable special solutions:

$$a = a_1 = \left(\frac{\alpha_x}{\alpha_y}\right)^{1/2}\left[\frac{K}{\kappa_{z0} - (\alpha_x + \sqrt{\kappa_{z0}})(\alpha_y + \sqrt{\kappa_{z0}})}\right]^{1/2},$$

$$b = b_1 = \left(\frac{\alpha_y}{\alpha_x}\right)^{1/2}\left[\frac{K}{\kappa_{z0} - (\alpha_x + \sqrt{\kappa_{z0}})(\alpha_y + \sqrt{\kappa_{z0}})}\right]^{1/2},$$

$$\theta(s) = \omega_1 s = \frac{\alpha_x\alpha_y}{\alpha_x + \alpha_y}s + \theta(0), \tag{19}$$

for branch A, and

$$a = a_2 = \left(\frac{\alpha_x + 2\sqrt{\kappa_{z0}}}{\alpha_y + 2\sqrt{\kappa_{z0}}}\right)^{1/2}\left[\frac{K}{\kappa_{z0} - (\alpha_x + \sqrt{\kappa_{z0}})(\alpha_y + \sqrt{\kappa_{z0}})}\right]^{1/2},$$

$$b = b_2 = \left(\frac{\alpha_y + 2\sqrt{\kappa_{z0}}}{\alpha_x + 2\sqrt{\kappa_{z0}}}\right)^{1/2}\left[\frac{K}{\kappa_{z0} - (\alpha_x + \sqrt{\kappa_{z0}})(\alpha_y + \sqrt{\kappa_{z0}})}\right]^{1/2},$$

$$\theta(s) = \omega_2 s = \frac{\alpha_x\alpha_y - 4\kappa_{z0}}{\alpha_x + \alpha_y + 4\sqrt{\kappa_{z0}}}s + \theta(0), \tag{20}$$

for branch B. In Eqs. (19) and (20), α_x and α_y are constant.

For branch A, the conditions for the confinement of corkscrewing elliptic beam equilibria are

$$\alpha_x/\sqrt{\kappa_{z0}} < 0, \quad \alpha_y/\sqrt{\kappa_{z0}} < 0,$$
$$(\alpha_x + \sqrt{\kappa_{z0}})(\alpha_y + \sqrt{\kappa_{z0}}) < \kappa_{z0} \tag{21}$$

for both positively and negatively charged particle beams. Because α_x and α_y have the same sign, the internal flow for branch A is always rotation like. For branch B, the conditions for the confinement of corkscrewing elliptic beam equilibria are

$$\alpha_y/\sqrt{\kappa_{z0}} > -2, \quad \alpha_x/\sqrt{\kappa_{z0}} > -2,$$
$$(\alpha_x + \sqrt{\kappa_{z0}})(\alpha_y + \sqrt{\kappa_{z0}}) < \kappa_{z0} \tag{22}$$

for both positively and negatively charged particle beams. In contrast to the internal flow for branch A, the internal flow

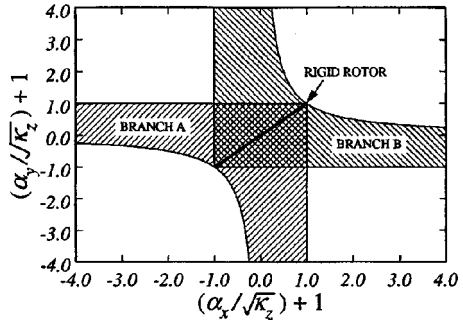

FIG. 2. Regions in parameter space for confinement of corkscrewing elliptic beam equilibria in a uniform magnetic field.

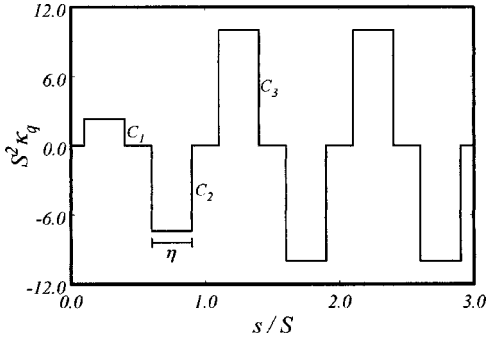

FIG. 3. Plot of the focusing parameter $S^2\kappa_q$ as a function of the propagation distance s.

for branch B can be either rotation like with α_x and α_y in the same sign or quadrupole flow like with α_x and α_y in apposite signs. Figure 2 shows the regions of the confinement of corkscrewing elliptic beam equilibria in a uniform magnetic field applicable for both positively and negatively charged particle beams. It is important to point out that the familiar cold-fluid round rigid-rotor beam equilibria [13,14] are recovered in the present analysis by setting $\alpha_x=\alpha_y$ in either Eq. (19) or Eq. (20), as indicated by the dark solid line shown in Fig. 2.

B. Control of halo formation and beam hollowing in ultrahigh brightness beams

As discussed in the Introduction, one of the key mechanisms for halo formation in high-intensity electron or ion beams is due to a mismatch in the particle phase-space distribution relative to an equilibrium distribution. In general, a distribution mismatch can lead to rather complex evolution in a beam, including not only halo formation, but also beam hollowing. This mechanism for halo formation and beam hollowing occurs for rms matched beams because rms beam matching does not necessarily guarantee the beam in an equilibrium state.

For example, both halo formation and beam hollowing were observed in the heavy ion beam injector experiment at Lawrence Berkeley National Laboratory (LBNL) [11], in which an ultrahigh-brightness, space-charge-dominated potassium ion beam was generated with an axisymmetric Pierce diode and then accelerated by a set of electrostatic quadrupoles. More recently, experimental evidence of beam hollowing was found in a high-brightness, space-charge-dominated electron beam experiment at University of Maryland [18].

As an important application of the equilibrium beam theory presented in Sec. IV, we develop and demonstrate a technique for controlling of beam halo formation and beam hollowing in ultrahigh-brightness beams. This technique is widely applicable in the design of ultrahigh-brightness beams and is effective before any collective instability develops to reach considerably large amplitudes.

To demonstrate the efficacy of this technique, we consider here a specific example, namely, the matching of a round particle beam generated by an axisymmetric particle source into alternating-gradient magnetic quadrupole focusing channel. For comparison, we analyze two nonrotating rms matched beams with the same intensity; one beam will be in equilibrium, and the other beam has an initial perturbation about the equilibrium transverse flow velocity. At the entrance of the alternating-gradient magnetic focusing channel ($s=0$), both beams have the same density profile defined in Eq. (15), but the transverse flow velocities of the beams are of the form [19]

$$\frac{d\mathbf{x}_\perp}{ds}=\frac{\mathbf{x}_\perp}{a}\left(\frac{da}{ds}\right)\left[1+\nu\left(1-\frac{2\mathbf{x}_\perp\cdot\mathbf{x}_\perp}{a^2}\right)\right], \tag{23}$$

where υ is a parameter that measures the nonlinearity in the velocity profile. For example, an initial velocity profile with $\nu>0$ in Eq. (23) may model the effects of the concave shape of a Pierce-type ion diode in the LBNL 2-MV Heavy Ion Beam Injector Experiment [11]. The value of υ in the LBNL experiment [11] is estimated to be $\nu=0.25$. For equilibrium beam propagation, $\nu=0$.

The rms matching for both beams with $\upsilon=0$ and 0.25 is obtained by numerically solving the rms envelope equations [5]

$$\frac{d^2\overline{a}}{ds^2}+\kappa_q(s)\overline{a}-\frac{K}{2(\overline{a}+\overline{b})}=0, \tag{24a}$$

$$\frac{d^2\overline{b}}{ds^2}-\kappa_q(s)\overline{b}-\frac{K}{2(\overline{a}+\overline{b})}=0, \tag{24b}$$

where $\overline{a}\equiv\langle x^2\rangle^{1/2}$ and $\overline{b}\equiv\langle y^2\rangle^{1/2}$ are the rms envelopes, $\langle\cdots\rangle$ denotes average over the particle distribution, and emittance terms are neglected. For given beam intensity K and focusing channel parameters C_3 and η shown in Fig. 3, we make use of Eq. (24) to determine the injection parameters for the axisymmetric beam, namely, $\overline{a}(0)$, $\overline{b}(0)$, $\overline{a}'(0)$, and $\overline{b}'(0)$, as well as the strengths of the two quadrupoles centered at $s=S/4$ and $s=3S/4$ in the first lattice, C_1 and C_2, as shown in Fig. 3, assuming all quadruples having the same width η and equally spaced. Because Eq. (24) has a unique solution for an rms matched beam in the constant-parameter alternating-gradient focusing section with $s/S>1$, integrating Eq. (24) from $s=S$ to $s=0$ yields four implicit functions $\overline{a}(C_1,C_2)$, $\overline{b}(C_1,C_2)$, $\overline{a}'(C_1,C_2)$, and $\overline{b}'(C_1,C_2)$. The conditions for an initially converging round beam, i.e., $\overline{a}(0)=\overline{b}(0)=a(0)/2=b(0)/2$ and $\overline{a}'(0)=\overline{b}'(0)$, uniquely determine the parameters C_1 and C_2, which is done numerically with Newton's method. The results are presented in Figs. 3 and 4.

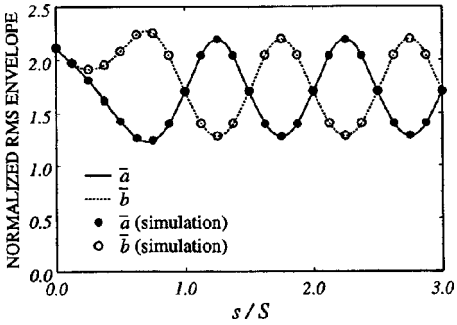

FIG. 4. Plots of rms beam envelopes versus propagation distances. Here the solid and dashed curves are obtained from Eq. (24), whereas the solid dots and open circles are from the self-consistent simulation for a beam with $\nu=0.25$. Here $\overline{a}$ and $\overline{b}$ are normalized to $\sqrt{\varepsilon(0)S}$.

Figure 3 shows the focusing field parameter $S^2\kappa_q$ as a function of s, where $\eta=0.3$, $C_1=2.31$, $C_2=7.44$, and $C_3=10.0$. In Fig. 4, the solid and dashed curves show, respectively, the rms matched envelopes $\overline{a}(s)$ and $\overline{b}(s)$ for the focusing channel with vacuum phase advance $\sigma_0=70.8°$ and beam perveance $SK/4\varepsilon(0)=16.0$ (corresponding to a space-charge-depressed phase advance of $\sigma=5.4°$), where a negligibly small unnormalized rms emittance of $\varepsilon(0)=0.15\times10^{-6}$ m rad has been assigned to the beam at $s=0$.

Self-consistent simulations are performed with $N_p=3072$ and free-space boundary conditions to study the phase space evolution for the two beams in the focusing channel shown in Fig. 3. In Fig. 4, the solid dots and open circles correspond to the rms envelopes $\overline{a}(s)$ and $\overline{b}(s)$ obtained from a self-consistent simulation for a beam initially with a nonlinear velocity profile with $\nu=0.25$. It is evident in Fig. 4 that there is excellent agreement between the prediction of the rms envelope equations (24a) and (24b) and the results of the self-consistent simulation, despite that the transverse flow velocity is perturbed substantially.

We now examine the evolution of the particle distribution if the nonlinearity in the initial transverse flow velocity profile is introduced and compare with equilibrium beam propagation. The results are summarized in Figs. 5 and 6. Figure 5 shows a comparison between particle distributions in the configuration space with and without nonlinearity in the initial transverse flow velocity at three axial positions: $s/S=0$, 1.0, and 2.5. These axial positions are chosen such that $\overline{a}(s)=\overline{b}(s)$. In Fig. 5, the plots shown on the left correspond to $\nu=0$ and those on the right to $\nu=0.25$. For $\nu=0.25$, the initially round beam develops sharp edges after the first lattice, becoming partially hollow subsequently at $s/S=2.5$. In Fig. 6(b), the radial distribution of 3072 macroparticles at $s/S=2.5$ shows that the density at the edge is twice the density at the center of the beam and that there is a small halo extending outward beyond the radius where the density reaches its maximum. The partially hollow density profile shown in Fig. 6(b) is similar to, but not as pronounced as, that observed in the heavy ion beam injector experiment at LBNL [11]. In contrast to the case with $\nu=0.25$, the beam propagates in an equilibrium state for $\nu=0$ without beam hollowing and without any significant beam halo formation, as shown in Fig. 6(a).

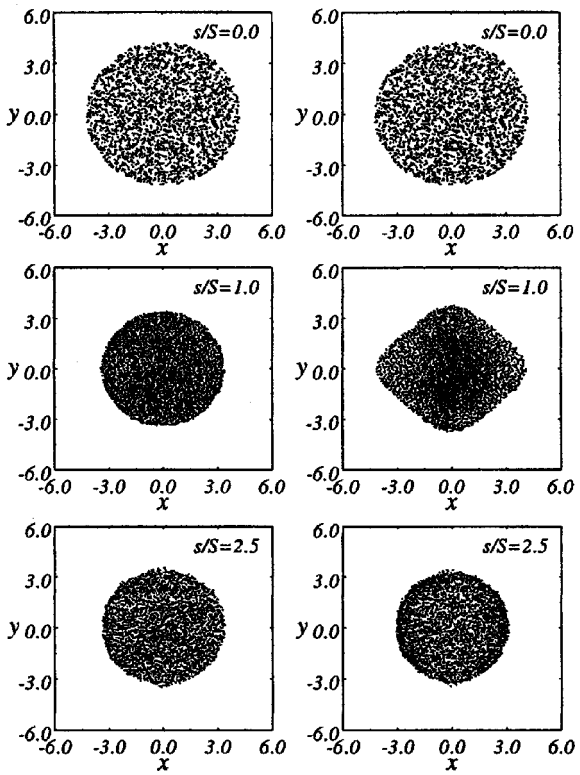

FIG. 5. Particle distributions in the configuration space for $\nu=0$ (left) and $\nu=0.25$ (right). Here the coordinates x and y are normalized to $\sqrt{\varepsilon(0)S}$.

C. Matching and transport of a beam into a periodic focusing channel consisting of overlapping solenoidal and quadrupole focusing fields

As another example of corkscrewing elliptic beam equilibrium, we consider the matching and transport of an initially round beam into a periodic focusing channel consisting

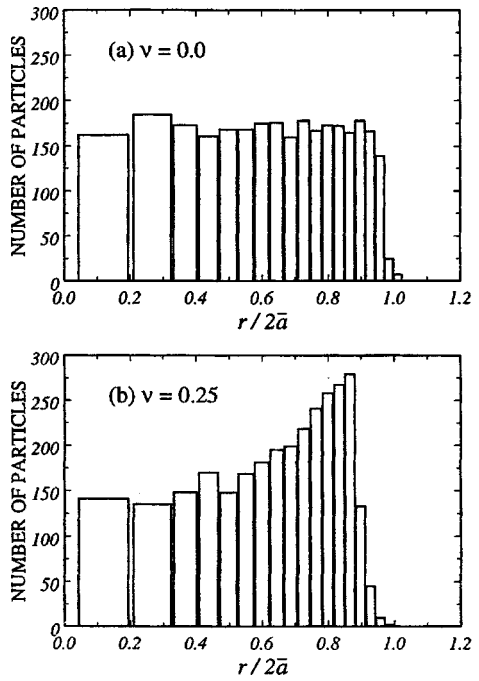

FIG. 6. Radial distribution of the macroparticles at $s/S=2.5$ for (a) $\nu=0$ and (b) $\nu=0.25$.

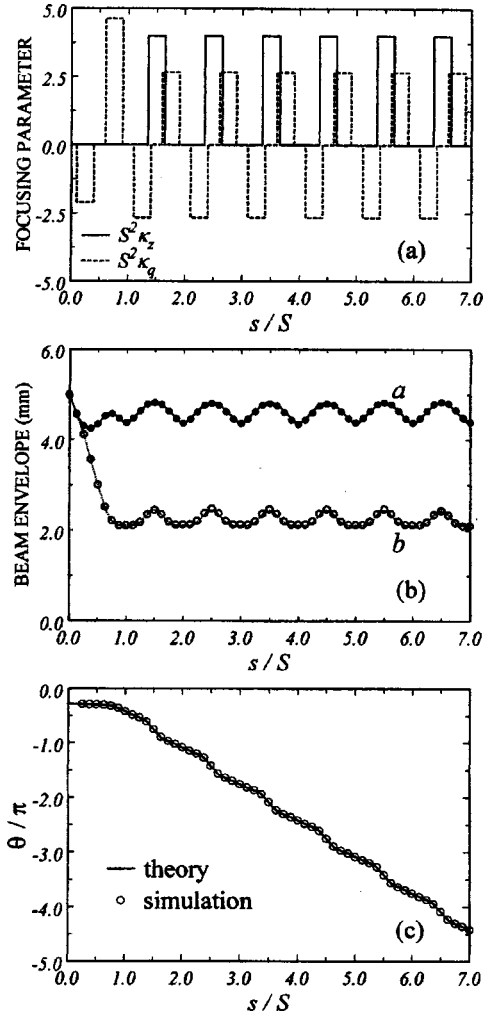

FIG. 7. Plots of focusing and beam parameters versus normalized propagation distance s/S for an equilibrium beam in a tapered linear focusing channel consisting of overlapping periodic solenoidal and alternating-gradient quadrupole magnetic fields. Here $K=1.6\times10^{-5}$ and $S=1.0$ m. In (a) the solid and dashed curves are dimensionless focusing parameters $S^2\kappa_z(s)$ and $S^2\kappa_q(s)$, respectively; in (b) the solid and dashed curves are the beam envelopes $a(s)$ and $b(s)$ predicted by Eq. (14), whereas the solid dots and open circles are obtained from the simulation; in (c) the solid curve and open circles are the angles of the beam ellipses obtained from Eq. (14) and the simulation, respectively.

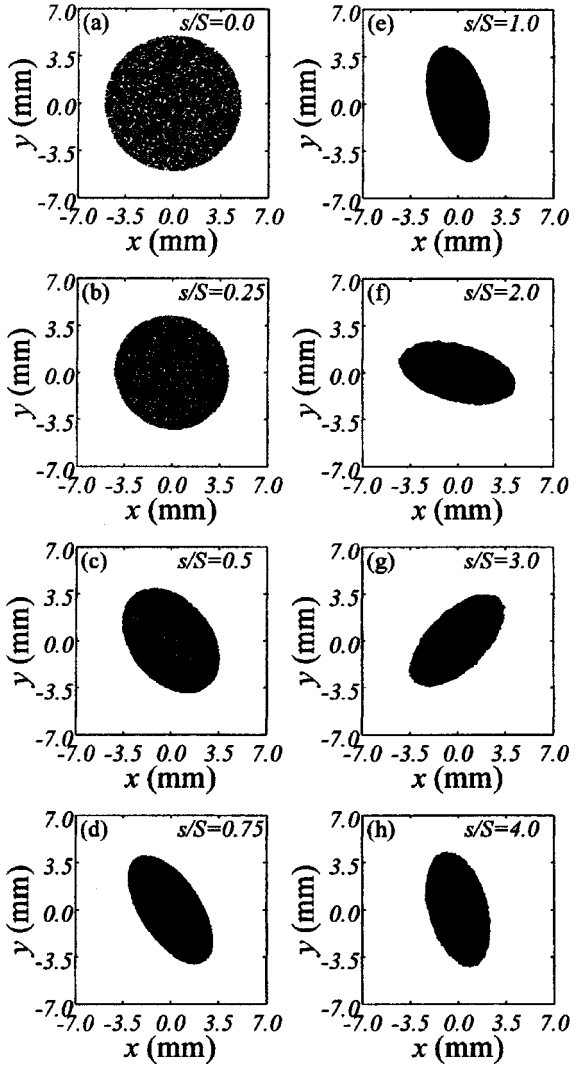

FIG. 8. Particle distributions in configuration space obtained from the simulation for the case shown in Fig. 7.

of overlapping solenoidal and quadrupole focusing fields. Figure 7(a) shows plots of dimensionless focusing parameters $S^2\kappa_z$ and $S^2\kappa_q$ versus propagation distance s/S for the channel. In Fig. 7(a), the width of solenoidal and quadrupole magnets is $0.3S$. In the matching section ($0<s<S$), two quadrupoles at $s/S=0.25$ and $s/S=0.75$ are placed at angles $\varphi_q=-50°$ and $\varphi_q=-40°$, respectively. In the periodic focusing section ($s>S$), the quadrupoles are placed at $\varphi_q=0°$ in the first cell ($1<s/S\leqslant2$) and are rotated by $-120°$ in each of subsequent cells, yielding a periodicity of $3S$ for the channel. To determine the angles and the strengths of the matching quadrupoles, we first find from Eq. (14) periodic solutions with $a(s+S)=a(s)$, $b(s+S)=b(s)$, $\alpha_x(s+S)=\alpha_x(s)$, $\alpha_y(s+S)=\alpha_y(s)$, and $\theta(s+3S)=\theta(s)$ in the periodic focusing section and then match the initially round beam with $a(0)=b(0)$ and $\alpha_x(0)=\alpha_y(0)$ with the periodic solution at $s/S=1$ using a shooting method. The results are shown in Fig. 7 for $K=1.6\times10^{-5}$ and $S=1.0$ m. The solid and dashed curves in Fig. 7(b) are calculated envelopes $a(s)$ and $b(s)$, and the solid curve in Fig. 7(c) is the angle $\theta(s)$.

We have validated the exact steady-state solutions using self-consistent simulations. In the simulations, use is made of Green's function method to determine electrostatic fields generated by the charged particles in the beam and image charges due to a perfectly conducting cylindrical tube of radius r_w. A detailed description of the simulation code was presented earlier [19]. For the focusing parameters shown in Fig. 7(a), 10^4 macroparticles are loaded in the present simulation according to the initial distribution function

$$f(\mathbf{x}_\perp,\mathbf{x}'_\perp)=n_b(x_\perp,0)\exp\{-[\mathbf{x}'_\perp\beta_b c-\mathbf{V}_\perp(\mathbf{x}_\perp,0)]^2/T(\mathbf{x}_\perp)\},$$

where $n_b(\mathbf{x}_\perp,0)$ and $\mathbf{V}_\perp(\mathbf{x}_\perp,0)$ are the initial density and velocity profiles defined in Eqs. (5) and (6), respectively, $T(\mathbf{x}_\perp)=T_0(x^2/a^2+y^2/b^2-1)$ is an effective temperature profile, and T_0 is a constant chosen to give an initial total (4 times rms) emittance of 0.2×10^{-6} m rad. The conducting cylindrical tube radius is chosen to be $r_w=10.0$ mm. Results of the simulation are summarized in Figs. 7(b), 7(c), and 8.

Shown in Figs. 7(b) and 7(c) is the excellent agreement between the beam envelopes $a(s)$ and $b(s)$ and angle $\theta(s)$ obtained from the self-consistent simulation and those predicted by the generalized beam envelope equations (14), as expected. In Fig. 8, particle distributions in the plane (x,y) are plotted at several axial locations of the matching section and the periodic focusing section, showing the transition from a round beam to a corkscrewing elliptic beam in the focusing channel. The elliptic beam completes a full clockwise turn from $s/S=1$ to $s/S=4$ [see Figs. 8(e)–8(h)]. Both image charge effects and emittance growth are negligibly small. The density profiles are computed at various axial locations in the simulation, and they are found in good agreement with the density profile defined in Eq. (5). It should be stressed that the beam propagates in a steady state without either beam hollowing or halo formation.

VI. CONCLUSIONS

We have shown that there exists a new class of cold-fluid corkscrewing elliptic beam equilibria for ultrahigh-brightness, space-charge-dominated beam propagation through a linear focusing channel consisting of uniform solenoidal, periodic solenoidal, and/or alternating-gradient quadrupole focusing magnets in an arbitrary arrangement including field tapering. Generalized beam envelope equations were derived. The equilibrium beam density and flow velocity profiles and equilibrium self-electric and self-magnetic fields were determined by solving generalized beam envelope equations. For beams with negligibly small emittance, these steady-state solutions were validated with self-consistent simulations using the Green's function method. While these steady-state solutions correspond to corkscrewing elliptic beam equilibria in general, they do recover many familiar beam equilibria in beam physics, such as the cold-fluid round rigid-rotor equilibrium and both the periodically focused rigid-rotor Vlasov equilibrium and Kapchinskij-Vladimirskij equilibrium in the zero-emittance limit.

Examples and applications of the present equilibrium beam theory were discussed. In particular, a corkscrewing elliptic beam equilibrium in a uniform solenoidal magnetic field was obtained. As an important application of the present equilibrium beam theory, a general technique was developed and demonstrated with an example to control large-amplitude density and flow velocity fluctuations (such as beam hollowing and halo formation) often observed in ultrahigh-brightness beams. Furthermore, an ultrahigh-brightness beam equilibrium in a periodic focusing channel consisting of overlapping solenoidal and quadrupole focusing field was obtained to illustrate a wide range of applicability of the present equilibrium beam theory in manipulating ultrahigh-brightness beams.

It is anticipated that the equilibrium beam theory presented in this paper can be used to perfectly match ultrahigh-brightness beams in practical beam transport systems and to design electron beam equilibrium configurations in new vacuum electronic devices. Finally, the present cold-fluid equilibrium theory can be generalized to include the effect of finite beam emittance, which will be discussed in a future article.

ACKNOWLEDGMENTS

This work was supported by the Department of Energy, Office of High Energy and Nuclear Physics Grant No. DF-FG02-95ER-40919, the Air Force Office of Scientific Research Grant No. F49620-97-1-0325 and No. F49620-00-1-0007, and in part by the Department of Energy through a subcontract with Princeton Plasma Physics Laboratory. The research by R.P. was also supported by CNPq, Brazil.

[1] J. Benford and J. A. Swegle, *High Power Microwaves* (Artech, Boston, 1992).
[2] E. D. Courant, M. S. Livingstone, and H. Snyder, Phys. Rev. **88**, 1190 (1952).
[3] *Space Charge Dominated Beams and Applications of High-Brightness Beams*, edited by S. Y. Lee, AIP Conf. Proc. No. 377 (AIP, New York, 1996).
[4] P. M. Lapostolle, IEEE Trans. Nucl. Sci. **NS-18**, 1101 (1971).
[5] F. J. Sacherer, IEEE Trans. Nucl. Sci. **NS-18**, 1105 (1971).
[6] D. Chernin, Part. Accel. **24**, 29 (1998).
[7] J. Barnard, in *Proceedings of the 1995 Particle Accelerators Conference* (Institute of Electrical and Electronics Engineering, Piscatoway, NJ, 1995, p. 3241.
[8] Q. Qian, R. C. Davidson, and C. Chen, Phys. Rev. E **51**, 3704 (1995).
[9] C. Chen and R. C. Davidson, Phys. Rev. Lett. **72**, 2195 (1994).
[10] R. L. Gluckstern, Phys. Rev. Lett. **73**, 1247 (1994).
[11] S. Yu, S. Eylon, E. Henestroza, and D. Grote, in *Space Charge Dominated Beams and Applications of High-Brightness Beams* [3], p. 134
[12] T. P. Wangler, K. R. Crandall, R. S. Mills, and M. Reiser, IEEE Trans. Nucl. Sci. **NS-32**, 2196 (1985).
[13] R. C. Davidson and N. A. Krall, Phys. Fluids **13**, 1543 (1970).
[14] A. J. Theiss, R. A. Mahaffey, and A. W. Trivelpiece, Phys. Rev. Lett. **35**, 1436 (1975).
[15] C. Chen, R. Pakter, and R. C. Davidson, Phys. Rev. Lett. **79**, 225 (1997).
[16] I. M. Kapchinskij, and V. V. Vladimirskij, in *Proceedings of the International Conference on High Energy Accelerators* (CERN, Geneva, 1959), p. 274.
[17] Equation (14) can be integrated numerically as a approaches b.
[18] S. Bernal, P. Chin, R. A. Kishek, Y. Li, M. Reiser, J. G. Wang, T. Godlove, and I. Haber, Phys. Rev. ST Accel. Beams **1**, 044202 (1998)
[19] M. Hess, R. Pakter, and C. Chen, in *Proceedings of the 1999 Particle Accelerator Conference*, edited by A. Luccio and W. Mackay (Institute of Electrical and Electronics Engineering, Piscatoway, NJ, 1989), p. 2752.